Molecular Insights Into the Binding of Linear Polyethyleneimines and single-stranded DNA using Raman Spectroscopy: A Quantitative Approach

Rusul Mustafa,[†] Maria Fitian,[‡] Nicholas B. Hamilton,[†] Jianing Li,[†] W. Ruchira Silva,[‡] and David Punihaole*,[†]

†Department of Chemistry, University of Vermont, Burlington, VT 05405 ‡Department of Chemistry and Biochemistry, Siena College, Loudonville, NY 12211

E-mail: David.Punihaole@uvm.edu

Abstract

Establishing how polymeric vectors such as polyethylenimine (PEI) bind and package their nucleic acid cargo is vital towards developing more efficacious and costeffective gene therapies. To develop a molecular-level picture of DNA binding, we examined how the Raman spectra of PEIs report on their local chemical environment. We find that the intense Raman bands located in the $1400 - 1500 \text{ cm}^{-1}$ region derive from vibrations with significant CH₂ scissoring and NH bending character. The Raman bands that derive from these vibrations show profound intensity changes that depend on both the local dielectric environment and hydrogen bonding interactions with the secondary amine groups on the polymer. We use these bands as spectroscopic markers to assess the binding between low molecular weight PEIs and single-stranded DNA (ssDNA). Analysis of the Raman spectra suggest that PEI primarily binds via electrostatic interactions to the phosphate backbone, which induces the condensation of the ssDNA. We additionally confirm this finding by conducting molecular dynamics simulations. We expect that the spectral correlations determined here will enable future studies to investigate important gene delivery activities, including how PEI interacts with cellular membranes to facilitate cargo internalization into cells.

Introduction

Developing non-viral vectors that safely and efficiently deliver exogenous nucleic acids into cells is essential for life science research and gene therapy applications. Polymers are an emerging and promising class of delivery vehicles since, unlike viral vectors, there is little risk of triggering life-threatening immune responses. ^{1,2} Cationic polyamines such as polylysine, polyornithine, and polyethylenimine (PEI) are among the most popular non-viral delivery vehicles. ³ Despite their popularity, however, the mechanisms by which these and other polymers interact with cells and nucleic acids to ensure successful delivery of their cargo remains poorly understood. For example, although it is considered a gold-standard in the field, PEI

still suffers from low transfection efficiency compared to viral vectors and exhibits relatively high cytotoxicity and non-biodegradability, which prevents its use in clinical applications.⁴

Polymer delivery vehicles perform important biological activities such as binding to the cell surface, entering cells via endocytosis, and delivering their nucleic acid cargo to the site-of-action within the cell. ^{1,2,5} One of the most important functions that polymers perform is the packaging of their nucleic acid cargo into complexes known as polyplexes. ⁶ The interactions between polymers and their cargo must be stable enough to prevent premature release outside the cell. ⁷ However, these interactions cannot be too stable to prevent efficient unpackaging and cargo release inside the cell. ^{1,8} Unfortunately, most of what is known about the interactions that stabilize polyplexes stems from structural data on the nucleic acid cargo and not the polymers. This incomplete picture makes it difficult to establish structure-activity relationships to rationally design more effective polymers for gene delivery applications. Thus, new tools are needed to investigate polyplex dynamics from both the perspective of the polymeric carrier and its cargo.

Cationic polyamines are thought to bind nucleic acids primarily through electrostatic interactions between their positively charged amino groups and the negatively charged phosphate backbone of nucleic acids.² Nuclear magnetic resonance (NMR) studies on small polyamines such as putrescine, spermidine, and spermine, for example, suggest that these molecules engage in transient, non-specific electrostatic interactions with the phosphate backbone of double-stranded DNA (dsDNA).^{9–11} These experimental results can be explained to varying degrees of success by polyelectrolyte, ^{12,13} Poisson-Boltzmann, ¹⁴ and counterion condensation theories, ¹⁵ all of which presume non-specific electrostatic interactions between the anionic DNA phosphate groups and the cationic polyamines. These binding models differ markedly from crystallographic studies, which indicate that spermine in particular preferentially binds specific, sequence-dependent sites on the major groove of dsDNA and may even promote the conversion of B-form DNA to A- or Z-form structures. ^{16–18}

More recent studies have utilized vibtrational spectroscopy methods such as infrared (IR)

absorption and Raman scattering to structurally characterize polyamine binding to nucleic acids. ^{19–21} These techniques are versatile methods to probe the nature of the binding interaction because they excite molecular vibrations that are intrinsically sensitive to the local chemical environment and structure of the chromophores being probed. By analyzing the frequency and intensity changes of specific vibrational marker bands, these studies demonstrate that low molecular weight polyamines such as spermidine and spermine preferentially bind dsDNA via electrostatic interactions with the phosphate backbone. However, these studies have mostly focused on analyzing the vibrational bands of dsDNA and not those of the polymers.

Here, we extend the work of these previous vibrational spectroscopic studies to examine nucleic acid binding by investigating how the Raman bands of cationic polyamines such as PEI report on local intermolecular interactions. We focus our studies on the compounds, Nethylpropylamine (NEPA), diethylenetriamine (DETA), triethylenepentamine (TEPA), and pentaethylenehexamine (PEHA), which are shown in Figure 1. We show that these molecules are excellent model systems since the internal monomers of PEHA and TEPA adopt similar conformations as those found in high molecular weight PEIs. We also demonstrate the Raman intensities of the CH_2 scissoring bands, found in the $1400-1500~\mathrm{cm}^{-1}$ region, sensitively report on the local electrostatic and hydrogen bonding interactions of the amine groups of PEIs. Using these bands as spectroscopic markers, we examine the structural changes that occur in both single-stranded DNA (ssDNA) and PEHA upon binding. Finally, we complement our Raman measurements with molecular dynamics (MD) simulations to develop a comprehensive, molecular-level picture of the complexation between PEIs and DNA. Ultimately, we anticipate that the spectroscopic markers discovered here can be utilized to monitor other activities that are important for the biological transport of nucleic acids by PEI polyplexes, including binding to the cell surface and intracellular release of cargo.

Experimental Methods

Materials. Acetonitrile (99.7% purity) was purchased from Alfa Aesar. Deuterated chloroform (CDCl₃), deuterated dimethyl sulfoxide ((CD₃)₂SO), and deuterium oxide (D₂O) were purchased at 99.9% purity from Cambridge Isotope Laboratories. Methanol (99.8% purity) was purchased from Acros Organics. Linear Polyethylenimine (2500 Da) was purchased from Polysciences, Inc. Pentaethylenehexamine (PEHA) and tetraethylenepentamine (TEPA) were purchased at 85–90% purity, while diethylenetriamine (DETA) was purchased at 99% purity from Sigma Aldrich. N-ethylpropylamine (NEPA) was purchased at 97% purity from Alfa Aesar. Oligonucleotides with the sequence GCACACATCGGACAGTTTGA were purchased from Synbio Technologies. All aqueous samples were prepared in MilliQ (18.2 MΩ) water.

Sample Preparation. To obtain a Raman spectrum of high molecular weight PEI, $0.075\,\mathrm{g}$ of polymer was dissolved in 1 mL methanol for a final concentration of 30 mM. To examine the coupling of vibrational modes, equimolar (200 mM) solutions of PEHA, TEPA, and DETA were prepared in water using acetonitrile as internal standard (1% v/v). To quantify the environmental sensitivity of NEPA in different solvents, samples were prepared in $\mathrm{H_2O}$, $\mathrm{D_2O}$, $\mathrm{CDCl_3}$, and $(\mathrm{CD_3)_2}\mathrm{SO}$ with a final concentration of 2.5% (v/v). For oligonucleotide binding studies, solutions of ssDNA (3 mM), PEHA (100 mM), and PEHA (100 mM)/ssDNA (3 mM) were prepared in water using acetonitrile as an internal standard (1% v/v).

Raman Spectroscopy. Raman spectra were measured using a home-built Raman spectrometer. Briefly, Raman spectra were excited using a 532 nm solid-state laser (Torus) purchased from Laser Quantum. The beam was reflected by a long-pass filter (LPD02-532RU-25X36X2.0, Semrock) and focused onto the sample with an infinity-corrected Olympus Ach $10\times/0.25$ NA objective. Typical laser powers used in our experiments ranged from 240 – 256 mW at the sample. The scattered light was collected using a 180° backscattering geometry and redirected through the long-pass filter into a refurbished Acton SpectroPro 2500i

spectrometer. The light was dispersed in the spectrometer using either a 600 gr/mm ruled or 2400 gr/mm holographic grating and then imaged using a PIXIS 400B CCD camera (Teledyne Industries). An achromatic quarter-waveplate (AQWP10M-580, Thorlabs Inc.) was placed before the spectrometer to minimize the polarization bias of the gratings, and the intensities were corrected using the IntelliCal system (Teledyne Industries). The nominal resolution of our spectrometer is ca. $2.6 \,\mathrm{cm}^{-1}$ at 435.8 nm using a 1200 gr/mm grating (Teledyne Industries). The acquisition times and frames collected varied depending on the sample and the concentrations used, but typically ranged between $1-120 \,\mathrm{s}$ per spectrum.

Spectral Processing and fitting. The measured Raman spectra were processed and spectrally peak-fitted using home-written MATLAB scripts. The spectra were first preprocessed by removing cosmic rays before averaging. The frequencies of all averaged spectra were calibrated against the 801.3, 1028.3, 1157.6, 1266.3, 1444.4, 2852.9, 2923.8, and 2938.3 cm⁻¹ bands of cyclohexane. In some cases, spectra needed to be additionally baseline-corrected due to a fluorescence background. The scripts used to process the spectra are provided in the supporting information (SI).

Computational Methods

Density Functional Theory (DFT) Calculations. We performed *ab initio* calculations to obtain optimized geometries and vibrational frequencies of NEPA, DETA, TEPA, and PEHA using unrestricted DFT with conductor-like polarizable continuum (CPCM) solvation models. DFT is a reliable and cost effective method to obtain the structure and vibrational frequencies of organic molecules such as NEPA. ^{22,23} As it gives accurate and widely accepted vibrational frequencies, we used the triple-split-valence basis set 6-311++G(d,p) with the B3LYP functional for the molecules examined here. ^{24,25} We compared the Raman frequencies of deuterated and non-deuterated species with experimental spectra after scaling them by a factor of 0.967. ²⁶ We also performed potential energy distribution (PED) analysis

for NEPA, DETA, TEPA, and PEHA molecules using VEDA software. ²⁷

MD simulations. The ssDNA model was constructed using w3DNA.²⁸ Fifteen PEHA molecules were then added to the box and placed at the edges, far from the single stranded DNA as to avoid any initial contacts. Half of the amines on these PEHA molecules were protonated in accordance with reported physiological conditions. ^{29,30} The dimensions of the box were set to (100, 75, 75) Å with the total box volume of 573 271 Å³. This volume corresponds to a ssDNA concentration of approximately 3 mM and a PEHA concentration of approximately 50 mM. The box was then filled with OPC³¹ water and Cl⁻ counterions were added into the model via the replacement method to neutralize the system. Our MD simulations were performed with a 9 Å cutoff for Van-der Waals interactions. The Particle-Mesh Ewald method 32 was used for approximating long-range interactions and the SHAKE 33 algorithm for all hydrogen constraints. Parameters for simulation were taken from the generalized amber forcefield (GAFF2) and OL15,³⁴ a force field for DNA-like molecules. Simulations were carried out with the $AMBER20^{35}$ molecular dynamics package. Initial steepest descent minimization was conducted with positional restraints on both the ssDNA and PEHA for 1000 steps to allow for water/ion relaxation. Two thousand steps of unrestrained minimization then followed. The model was then slowly heated from 100 K to 300 K over the course of a 250 ps equilibration simulation. MD in an NPT ensemble was then performed for a simulation time of 50 ns. Simulations were analyzed with in-house python scripts utilizing the MDA nalysis 36,37 package. The VMD 38 program was used for visualization. The GRO-MACS³⁹ package was also utilized for periodic boundary conditions and solvent accessible surface area calculations.

Results and Discussion

Raman spectra of high molecular weight PEI. High molecular weight PEIs are typically employed in gene delivery applications due to their high transfection efficiency. 40

Since high molecular weight PEIs are not very soluble in water, 41 we measured the Raman spectrum of linear PEI (2500 Da) in methanol at room temperature. The bands observed in our spectrum agree well with reported FTIR 42 and surface-enhanced Raman spectra. 43 The spectrum, shown in Figure 2, is dominated by strong bands in the 2700 – 3000 cm $^{-1}$ and 1400-1500 cm $^{-1}$ regions. Additional weaker spectral features, however, appear between 1000-1400 cm $^{-1}$ region. The bands between 2700-3000 cm $^{-1}$ are readily assigned to the CH $_2$ asymmetric and symmetric stretching modes. The bands located in the region near ca. 1455 cm $^{-1}$ have been previously assigned to vibrations that contain both CH $_2$ scissoring and NH in-plane bending character, while the weaker bands in the 1200-1400 cm $^{-1}$ region have been attributed to CH $_2$ wagging and twisting modes. 42 The weak features between 1000-1200 cm $^{-1}$ have been assigned to C-N stretching vibrations. 42 These bands, however, are difficult to see in our spectrum because they overlap with the intense C-O stretching band of methanol. 44

Raman spectra of low molecular weight PEIs. To develop a detailed understanding of the vibrational spectra for ethylenimine systems, we investigated the small molecule model compounds, NEPA, DETA, TEPA, and PEHA (Figure 1). Figure 3a-c shows the Raman spectra of PEHA, TEPA, and DETA. Similar to high molecular weight PEI, the spectra shown in Figure 3 show strong CH₂ stretching bands in the 2700 – 3000 cm⁻¹ region, as well as spectral features in the fingerprint region between 1000 – 1500 cm⁻¹. To analyze the fingerprint region in more detail, we used DFT calculations to help guide us in assigning the Raman spectra of PEHA, TEPA, and DETA. Our assignments are shown in Table 1, and they are overall in good agreement with previously published Raman studies on related polyamines such as spermidine and spermine. ¹⁹⁻²¹

Based on our DFT calculations (see Tables S1-S3, Figure S1), the strong Raman bands located in the $1400-1500~\rm cm^{-1}$ derive from vibrations that contain significant contributions of in-plane NH bending and CH₂ scissoring motions. The Raman bands located in the region between $1300-1400~\rm cm^{-1}$ can be assigned to vibrations that are comprised mainly of CH₂

wagging. The vibrational modes between $1000 - 1200 \text{ cm}^{-1}$ contain significant contributions of CH_2 twisting character. Interestingly, the band at ca. 1205 cm^{-1} appears only in TEPA and PEHA, but not in DETA. This mode can be assigned to a predominately CH_2 twisting vibration.

Although the Raman spectra of PEHA, TEPA, and DETA closely resemble that of high molecular weight PEI, they do contain noticeable differences. For example, the 1000 – 1300 cm⁻¹ region in the spectra of PEHA, TEPA, and DETA (Figure 3a-c) contain additional Raman bands compared to the spectrum of high molecular weight PEI (Figure 2). These additional bands presumably derive from the terminal monomers, whose spectroscopic contributions are negligible in high molecular weight PEIs. ⁴² The Raman spectrum of DETA (Figure 3c) most closely approximates the spectrum of the terminal monomers since it is the smallest molecule (Figure 1). In contrast, the PEHA (Figure 3a) and TEPA (Figure 3b) spectra contain greater spectroscopic contributions of the internal monomers. Since the solutions of the compounds were prepared at equimolar concentrations, the difference spectrum between PEHA and TEPA should closely approximate the Raman spectrum of internal monomers observed for high molecular weight PEI, assuming there is negligible coupling of vibrations between the monomer subunits. Similar assumptions have been made to interpret the vibrational spectra of polypeptides in extended or disordered conformations. ^{45,46}

To calculate the difference spectrum, we first normalized the minuend (PEHA) and the subtrahend (TEPA) to the nitrile stretching band (ca. 2250 cm⁻¹) of acetonitrile, which we used as an internal intensity standard. As seen in Figure 3d, the difference spectrum does indeed closely resemble the spectrum of high molecular weight PEI, exhibiting both the strong band centered at ca. 1460 cm⁻¹, as well as weaker features between 1000 – 1300 cm⁻¹ that derive from CH₂ twisting and wagging modes. The fact that the PEHA - TEPA difference spectrum closely resembles the spectrum shown in Figure 2 indicates that the internal monomers of small PEIs such as PEHA and TEPA adopt a similar distribution of conformations and sense similar local chemical environments as the monomer subunits of

high molecular weight PEI. This also indicates that low molecular weight molecules such as PEHA and TEPA can serve as useful model systems to conduct detailed investigations into the spectroscopic behavior of PEIs.

In addition to this, the Raman spectra of PEHA and TEPA can reasonably be modeled as a linear combination of the DETA spectrum and the PEHA - TEPA difference spectrum (red traces in Figure 3a and b). The subtle differences observed in the modeled and experimental spectra derive from imperfections associated with applying baseline corrections in the raw PEHA and TEPA spectra due to their fluorescence backgrounds. The ability to reasonably model these spectra as the summed contributions of internal and terminal monomers reinforces the validity of the local-mode behavior of the vibrations in PEIs.

This result significantly simplifies the analysis of PEI Raman spectra. This is because any spectral frequency and intensity changes observed in PEIs do not result from confounding vibrational coupling phenomena that give rise to "excitonic" frequency splitting behavior and changes in band intensities due to energy transfer. ^{45,46} Thus, the band intensities observed in the Raman spectra of PEIs can simply be analyzed in the context of changes in the Raman polarizability of vibrational modes due to the local conformation adopted or chemical environment felt by the monomer subunits.

Raman spectra of NEPA. Armed with this insight, we investigated how the Raman bands of PEIs report on interactions with their local chemical environment. Since the vibrations are localized, we used NEPA (Figure 1) as a small molecule model compound for these studies. NEPA is the simplest model compound for PEI since it best approximates the chemical structure of the monomer subunits. The Raman spectra of NEPA in both H₂O and D₂O are shown in Figure 4. The spectrum of NEPA in H₂O (Figure 4a) shares similar spectroscopic features as those shown in the spectra presented in Figures 2 and 3. To the best of our knowledge, the vibrational band assignments for NEPA have not been reported previously. Therefore, to verify that the vibrational modes are similar in normal mode composition to those of PEIs, we performed a normal mode analysis using DFT calculations

(Figure S2 and S3).

The results from our normal mode analysis are shown in Table S4. Overall, our analysis indicates that many of the vibrations in the fingerprint region are similar in normal mode composition as their PEI counterparts. One notable difference, however, is that the PEDs of several NEPA modes contain significant contributions (> 10%) of CH₃ wagging or twisting motions. This creates a more complex spectral pattern in the $1400-1500~\rm cm^{-1}$ region. Whereas our normal mode calculations indicate that DETA, TEPA, and PEHA exhibit one dominant band deriving from a CH₂ scissoring and NH bending vibration, the calculated spectrum of NEPA shows several bands (Figures S1 - S3). Importantly, however, the most intense bands in $1400-1500~\rm cm^{-1}$ for NEPA still derive from vibrations that contain significant CH₂ scissoring and NH in-plane bending character. The contribution of NH motion to these vibrations in NEPA is confirmed, as evidenced by the noticeable spectral intensity changes that occur in this region upon N-deuteration (Figure 4b).

Given their significant NH bending character, we hypothesized that the CH₂ scissoring Raman bands can be used to monitor local chemical environmental characteristics of NEPA and PEI. The rationale for our hypothesis is based on several lines of evidence from the literature. The first line stems from Hashida et al.,⁴⁷ who performed a study examining the hydration dependence of the IR absorption bands of PEI. Their IR spectra show profound intensity changes in the 1400 – 1500 cm⁻¹ region of PEI as a function of hydration, which they do not comment on. The second line of evidence stems from studies, which show that CH₂ scissoring Raman bands of lipids and polymers such as polyethylene report on the lateral packing of their aliphatic chains.^{48–50} Finally, a third line of evidence stems from a recent paper by Kurouski and coworkers,⁵¹ who suggest that the CH₂ scissoring Raman bands are additionally sensitive to the local conformation of the aliphatic chains of plant waxes. Building upon these studies, we set out to further investigate the environmental sensitivity of the CH₂ scissoring modes of PEIs. We discuss in detail how these vibrations report on intermolecular interactions below.

Environmental Sensitivity of the CH₂ scissoring modes. There are several methods to investigate the sensitivity of a vibrational marker to its local chemical environment. For simple vibrations such as pure stretching modes (e.g. C=O), a common method is to measure the frequency shifts in different solvents that vary in properties such as polarity, donor/acceptor number, or hydrophobicity. ^{52–54} The measured frequency shifts can then be correlated to solvent dielectric constants or other empirical polarity parameters. These correlations can then, in turn, be used to formulate Badger-Bauer-type relationships that map frequency shifts to changes in the interaction energies between specific functional groups of molecules and their local environment. ^{55,56} For vibrations with more complex eigenvector compositions, however, the frequency dependence on different solvent properties may be small or difficult to interpret. In these situations, the sensitivity of the vibrational marker to its local environment can also be assessed by quantifying changes in Raman scattering cross sections under different solution conditions. ^{57,58}

Compared to gas phase, the differential scattering cross section of a vibrational mode for a molecule in solution, $(d\sigma_i/d\Omega)_{soln}$, is:^{59,60}

$$\left(\frac{d\sigma_i}{d\Omega}\right)_{soln} = L\left(\frac{d\sigma_i}{d\Omega}\right)_{gas} \tag{1}$$

where $(d\sigma_i/d\Omega)_{gas}$ is the differential cross section of the mode for the molecule in the gas phase. The scattering cross section is directly proportional to the change in the polarizability of the mode along its vibrational normal coordinates $(\partial \alpha_i/\partial Q_i)$. ⁶¹ The proportionality factor, L, corrects the solution phase cross sections for the influence of intermolecular interactions on the Raman polarizability and/or dielectric effects due to the local solvent reaction field. ^{62,63} When only dielectric effects are considered, the correction factor can be written as: ^{59,60}

$$L = \left(\frac{n^2 + 2}{3}\right)^4 \tag{2}$$

where n is the refractive index of the solvent at the laser excitation wavelength (532 nm). It

is important to note that eq. 2 is valid only in cases where the optical dispersion is small, such as in the case of the non-resonance Raman measurements made here.

According to eq. 1, the ratio of the cross sections in two different solvents, j and k, should equal 1 if the local correction factors are taken into account:

$$\frac{L_j}{L_k} \frac{(d\sigma_i/d\Omega)_k}{(d\sigma_i/d\Omega)_j} = 1 \tag{3}$$

Eq. 3 is valid only if dielectric effects due to non-specific electrostatic interactions influence the Raman cross sections. Significant deviations from unity in eq. 3 indicates that specific intermolecular interactions, such as hydrogen bonding, are occurring.⁶⁰

Using this theory as a guide, we set out to determine how the differential Raman cross sections of the $1400-1500~{\rm cm^{-1}}$ modes change in ${\rm H_2O}$, ${\rm CDCl_3}$, and ${\rm (CD_3)_2SO}$ (see SI for details and Figures S4-S7). We chose these solvents because they vary in their dielectric and hydrogen bonding properties: ${\rm H_2O}$ possesses a high dielectric constant $(\epsilon_r \sim 80)^{64}$ and can act as both a hydrogen bond donor and acceptor for polyamines; ${\rm (CD_3)_2SO}$ possesses an intermediate dielectric constant $(\epsilon_r \sim 46.7)^{65}$ and acts as a hydrogen bond acceptor; and ${\rm CDCl_3}$ possesses a low dielectric constant $(\epsilon_r \sim 4.81)^{65}$ and is not expected to strongly interact with polyamines.

Table 2 lists the values of the differential Raman scattering cross sections of NEPA in these solvents. As seen in the table, the cross sections of the two modes centered near $1450\,\mathrm{cm^{-1}}$ are the largest, ranging between ca. $4.9\times10^{-4}\,\mathrm{mb\,sr^{-1}}\,\mathrm{molec.^{-1}}$ in CDCl₃ to $9.9\times10^{-4}\,\mathrm{mb\,sr^{-1}}\,\mathrm{molec.^{-1}}$ in H₂O. Compared to $(\mathrm{CD_3})_2\mathrm{SO}$, the differential cross sections of NEPA in CDCl₃ are all smaller. In addition, with the exception of the ca. 1443 and $1483\,\mathrm{cm^{-1}}$ modes, the cross sections of the 1467, 1455, and $1448\,\mathrm{cm^{-1}}$ modes are also smaller or similar in $(\mathrm{CD_3})_2\mathrm{SO}$ compared to H₂O. Based on these results, it is clear that the CH₂ scissoring Raman bands of NEPA generally decrease in intensity going from high to low dielectric environments.

These results suggest that the Raman intensities of the CH_2 scissoring modes report, in

part, on the local dielectric environment. To assess if dielectric effects are solely responsible for the observed intensity changes, we also determined the cross sections ratios for CDCl₃ to $(CD_3)_2SO$ and $(CD_3)_2SO$ to H_2O calculated using eq. 3. As seen in Table 2, the cross section ratios (after correcting for dielectric effects) for CDCl₃ to $(CD_3)_2SO$ exhibit values between 0.7-0.8. In contrast, the ratios for $(CD_3)_2SO$ to H_2O exhibit a more complex behavior. For example, the ca. 1443 and 1483 cm⁻¹ modes exhibit ratios that are close to 1. However, the ratios for the ca. 1448, 1455, and 1467 cm⁻¹ modes range between 0.3-0.7.

The uncertainties in the cross section ratios are reported in Table 2. They stem primarily from the uncertainties in the band cross sections from fitting the NEPA spectra (see SI for details). As seen in Table 2, the deviations from unity are significant for all the ratios that we calculated. We determined the cross sections by referencing the band intensities to the known cross section of the nitrile stretching mode of acetonitrile (see SI for details), which was originally measured by Dudik et al. ⁶⁶ The authors of this study report that the uncertainty in their cross section measurements were less than 20%. Even if this uncertainty is factored in, only the $(CD_3)_2SO$ to H_2O ratios that correspond to the 1443 and 1483 cm⁻¹ modes are close to unity. Thus, the calculated cross section ratios indicate that, in general, dielectric effects alone are insufficient to describe the observed Raman intensity changes of NEPA in H_2O and $(CD_3)_2SO$ compared to $CDCl_3$.

One reason for the discrepancies in the cross section ratios for the ca. 1448, 1455, and $1468\,\mathrm{cm^{-1}}$ modes is that they contain significant NH bending character. This enables these modes to sense hydrogen bonding interactions between $\mathrm{H_2O}$ and $(\mathrm{CD_3})_2\mathrm{SO}$ molecules with NEPA. The sulfoxide group of $(\mathrm{CD_3})_2\mathrm{SO}$ acts as a hydrogen bonding acceptor for the NH group of NEPA and other polyamines. In contrast, the oxygen atom of $\mathrm{H_2O}$ can accept a hydrogen from the amine group of NEPA or donate its hydrogen to the amine lone pair. These hydrogen interactions distort the ground state structure of NEPA such that $(\partial \alpha_i/\partial Q_i)$ presumably increases for the ca. 1448, 1455, and 1468 cm⁻¹ modes. This consequently increases their respective cross sections and results in their Raman bands being more intense

in the $(CD_3)_2SO$ and H_2O spectra compared to the spectrum of NEPA in $CDCl_3$.

PEI-DNA Binding Interactions. We capitalized on the environmental sensitivity of the CH₂ scissoring modes to probe the binding of PEIs to ssDNA. Previous studies by Deng et al., ¹⁹ as well as Ramìrez and coworkers, ^{20,67} used Raman spectroscopy to investigate the binding of spermine, spermidine, and putrescine to dsDNA. However, these studies focused exclusively on analyzing changes in the Raman bands of DNA to investigate conformational changes due to polyamine binding. The consensus between these studies is that polyamine binding is mediated primarily through non-specific electrostatic interactions as observed from perturbations in the phosphodiester stretching modes of dsDNA. We expanded upon these studies to probe binding from the point of view of the polymer to gain additional or complementary insights.

Figure 5 shows the Raman spectra of ssDNA (Figure 5c), PEHA (Figure 5b), and ssDNA and PEHA mixed together in solution (Figure 5a). The spectrum of ssDNA (Figure 5c) shows many features in the fingerprint region between 700 – 1600 cm⁻¹ that can be assigned to vibrations from the nucleotide bases, as well as the phosphate and deoxyribose backbones. We used previous studies by Peticolas and Benevides et al. 68,69 as a guide to assign these bands (Table S5). The 700 – 1300 cm⁻¹ region can be assigned to vibrations from cytosine, thymine, and the phosphate backbone. Similarly, the 1300 – 1400 cm⁻¹ region shows Raman bands that derive from vibrations of the thymine, adenine, and guanine bases. The 1400 – 1500 cm⁻¹ can be assigned to features that derive from guanine and adenine modes.

The spectrum of the PEHA and ssDNA mixture in solution is shown in Figure 5a (black trace). The spectrum shows significant changes compared to the spectra of only ssDNA (Figure 5c) or PEHA (Figure 5b) in solution. Among the most important spectral changes that we observe is a downshift of the phosphodioxy (PO_2^-) stretching mode of ssDNA to $1088\,\mathrm{cm}^{-1}$ (Table S5). This downshift indicates that the phosphate groups of the ssDNA are engaged in electrostatic interactions, consistent with the findings by Deng $et~al.^{19}$ and Ramìrez and coworkers 20,67 for dsDNA. The PEHA-ssDNA spectrum also exhibits noticeable

intensity differences in the Raman bands compared to the spectra of only PEHA and ssDNA. Importantly, these intensity differences are not due to the spectral overlap of the PEHA and ssDNA bands, as indicated by the fact that the PEHA-ssDNA spectrum cannot be modeled as a linear combination of the PEHA and ssDNA spectra (red trace in Figure 5a). This indicates that the vibrational Raman cross sections change significantly for PEHA and ssDNA due to complexation.

To highlight the intensity changes that occur because of complexation, we first normalized the experimental spectra shown in Figure 5a-c to the 2250 cm⁻¹ nitrile stretching band of acetonitrile. We then subtracted the modeled spectrum (red trace) from the PEHA-ssDNA spectrum (black trace). The resulting difference spectrum (Figure 5d) shows noticeable negative features between ca. 1050 - 1120 cm⁻¹, which are broad and poorly resolved. These features can be attributed to vibrations localized to the phosphate backbone, which are known to be sensitive to the conformations of nucleic acids. The decrease in the intensity of these bands may be due to a hypochromic effect that indicates PEHA binding to the phosphate backbone condenses or collapses the ssDNA.^{68,70}

The difference spectrum also shows a strong negative feature centered at ca. $1460\,\mathrm{cm^{-1}}$. This feature could possibly be assigned to vibrations localized to the deoxyribose phosphate backbone, adenine, or guanine moieties of the ssDNA. Several studies report that the Raman bands corresponding to these modes show only a modest sensitivity to DNA structure. These bands do not significantly exhibit intensity changes when DNA changes from a B-form to a disordered structure. In contrast, these bands increase in intensity for B- to A-form DNA structural transitions. 68,71,72 Since the ssDNA is already structurally disordered, we do not expect the ssDNA bands in this region to significantly change upon binding to PEHA molecules. We therefore assign the negative feature at $1460\,\mathrm{cm^{-1}}$ to the CH₂ scissoring modes of PEHA. Based on our studies discussed above, the decrease in the intensity of the CH₂ scissoring bands likely derives from the hydrogen bonding and electrostatic interactions between PEHA and ssDNA. The relative dielectric constant (ϵ_r) of water is 80 and 8 for

DNA.⁷³ Thus, PEHA experiences a change from a high to low dielectric environment going from its unbound state to binding the surface of the ssDNA. Taken together with the changes observed in the ssDNA spectra, our interpretation of the data suggests that PEHA primarily binds ssDNA through electrostatic interactions via the phosphate backbone, as well as possible hydrogen bonding interactions with the nucleobases. These binding interactions concomitantly induce the condensation of the ssDNA.

To validate this interpretation, we conducted MD simulations to monitor the binding between PEHA and ssDNA (see Computational Methods for details). We examined the interactions between PEHA molecules and ssDNA by measuring contacts within a 4 Å cutoff between the polymer and both the backbone and nucleobase atoms of interest. Specifically, all hydrogen bond donors and acceptors were chosen for the bases, while the charged phosphate groups were selected for the backbone. Contacts were measured between these atoms and the six amines present in each PEHA moiety. The number of contacts between the PEHA and the ssDNA molecules were then averaged per frame and residue and plotted.

Our MD simulation results were consistent with our interpretation of the Raman spectra. The simulation shows that PEHA establishes a high overall binding affinity (66% of polymer bound to ssDNA surface) and a defined preference for electrostatic contacts with the DNA backbone over hydrogen bonding to the ssDNA bases (Figure 6a). We examined the electrostatic surface potential of the ssDNA and projected for visualization. Multiple hot spots appeared on the ssDNA face and were subsequently occupied by the PEHA (Figure S8a). As expected, the high potential surface appeared continuous throughout the backbone, folding the neutral nucleobases inside the molecule and exposing the charged phosphate groups, which PEHA molecules have access to bind. The 5' end of the ssDNA was shown to have the most active bases, with those near 3' end of the molecule overwhelmingly recruiting PEHA via electrostatic interactions (Figure 6b). This is likely due to the disordered ssDNA folding back upon itself in the simulation (Figure 6a, Figure S8). This conformational change likely internalizes some of the nucleotides near the 3' end, while leaving the bases near the 5' end

of the ssDNA strand exposed to bind PEHA. This hypothesis is consistent with the overall contact heatmap (Figure S8b), which highlights higher PEHA binding affinity towards each end of the ssDNA and a lower affinity for the middle of the molecule.

Conclusion

We examined the environmental sensitivity of the Raman spectra of PEI to investigate its binding to ssDNA. Our DFT calculations and Raman spectroscopic measurements indicate that NEPA, as well as PEHA, TEPA, and DETA, are good model systems to study the spectroscopic behavior of PEIs in different chemical environments. Our data indicate that the internal monomers of PEHA and TEPA adopt similar conformations as high molecular weight PEIs. We also show that the spectra of PEIs can be accurately modeled as a linear summation of the spectral contributions of their internal and terminal monomers. This indicates the absence of vibrational coupling between adjacent monomers. Importantly, this result significantly simplifies the analysis of PEI spectra since intensity and frequency changes can be attributed solely to differences in the local chemical environment.

We also show that the Raman bands found in the $1400 - 1500 \text{ cm}^{-1}$ region are excellent spectroscopic markers to monitor the local interactions and structural dynamics of PEIs. Our DFT calculations and N-deuteration studies indicate that these bands derive from vibrations, which contain significant CH_2 scissoring and NH bending character. Overall, the Raman intensities of these bands decrease significantly going from high to low dielectric environments. However, sensitivity of the scattering cross sections of these modes to different chemical environments cannot be understood solely in terms of local dielectric effects. Hydrogen bonding interactions between the secondary amine groups and their local environment also significantly affect the scattering cross sections of these vibrations.

Using the environmental sensitivity of the CH₂ scissoring modes, we investigated the binding of PEIs to ssDNA. Our Raman spectroscopic measurements indicate that PEI binds

ssDNA via hydrogen bonding interactions, as well as electrostatic interactions with the phosphate backbone. These interactions consequently condense the ssDNA. The conclusions drawn from our Raman measurements are qualitatively reinforced by MD simulations, which additionally show that PEI exhibits a distinct preference towards electrostatic over hydrogen bonding interactions with ssDNA. We expect that this work will pave the way toward more sophisticated studies of high molecular weight PEI, as well as other cationic polyamines used in gene delivery applications. We anticipate, for example, that the spectroscopic markers identified here can be used to investigate the molecular interactions between PEI gene delivery vehicles and cellular membranes, which facilitate uptake and endocyotosis. Given the localized nature of these modes, we believe that perdeuteration of the aliphatic carbons of PEI can provide a way to distinguish these Raman bands from those of lipids without significantly altering their spectroscopic behavior and environmental sensitivity. These fundamental insights will greatly benefit the field of polymer gene delivery since it will provide a detailed understanding of the cellular mechanism of PEI vectors on a molecular level. This would ultimately assist in developing more efficient polymer-based delivery vectors that could reach clinical translations.

Acknowledgement

We thank Madeline Hatch, Samantha Stanhope, and Jessica Caruso for useful conversations. Funding for this work was provided by the University of Vermont (DP and RM). Funding was also provided by the National Institutes of Health, R01-GM129431 (JL and NBH), as well as P20 GM1350007 through the Vermont Center for Cardiovascular and Brain Health pilot grant award (DP and RM). Raman spectra were measured using equipment donated by the Physics Department at the University of Vermont, or purchased from funds provided by the Spectroscopy Society of Pittsburgh (DP). DFT calculations were performed using the Siena College High Performance Computing Center (WRS and MF).

Supporting Information Available

Tables S1-S5 and Figures S1-S8. Description of peaking fitting methods, differential Raman cross section calculations, DFT calculation files, and MATLAB scripts for processing data.

References

- (1) Kumar, R.; Santa Chalarca, C. F.; Bockman, M. R.; Bruggen, C. V.; Grimme, C. J.; Dalal, R. J.; Hanson, M. G.; Hexum, J. K.; Reineke, T. M. Polymeric Delivery of Therapeutic Nucleic Acids. *Chem. Rev.* 2021, 121, 11527–11652.
- (2) Wong, S. Y.; Pelet, J. M.; Putnam, D. Polymer systems for gene delivery—Past, present, and future. *Prog. Polym. Sci.* **2007**, *32*, 799–837.
- (3) Boussif, O.; Lezoualc'h, F.; Zanta, M.; Mergny, M.; Scherman, D.; Demeneix, B.; Behr, J. A versatile vector for gene and oligonucleotide transfer into cells in culture and in vivo: polyethylenimine. *Proc. Natl. Acad. Sci. U.S.A.* **1995**, *92*, 7297–7301.
- (4) Zakeri, A.; Kouhbanani, M. A. J.; Beheshtkhoo, N.; Beigi, V.; Mousavi, S. M.; Hashemi, S. A. R.; Zade, A. K.; Amani, A. M.; Savardashtaki, A.; Mirzaei, E. et al. Polyethylenimine-based nanocarriers in co-delivery of drug and gene: a developing horizon. *Nano Reviews Experiments* 2018, 9, 1488497.
- (5) Van Bruggen, C.; Hexum, J. K.; Tan, Z.; Dalal, R. J.; Reineke, T. M. Nonviral Gene Delivery with Cationic Glycopolymers. *Acc. Chem. Res.* **2019**, *52*, 1347–1358.
- (6) Ma, K.; Mi, C. L.; Cao, X. X.; Wang, T. Y. Progress of cationic gene delivery reagents for non-viral vector. *Appl. Microbiol. Biotechnol.* **2021**, *105*, 525–538.
- (7) Bruggen, C. V.; Punihaole, D.; Keith, A. R.; Schmitz, A. J.; Tolar, J.; Frontiera, R. R.; Reineke, T. M. Quinine copolymer reporters promote efficient intracellular DNA deliv-

- ery and illuminate a protein-induced unpackaging mechanism. *Proc. Natl. Acad. Sci. U.S.A.* **2020**, *117*, 32919–32928.
- (8) Bus, T.; Traeger, A.; Schubert, U. S. The great escape: how cationic polyplexes overcome the endosomal barrier. *J. Mater. Chem. B* **2018**, *6*, 6904–6918.
- (9) Wemmer, D. E.; Srivenugopal, K. S.; Reid, B. R.; Morris, D. R. Nuclear magnetic resonance studies of polyamine binding to a defined DNA sequence. J. Mol. Biol. 1985, 185, 457–459.
- (10) Padmanabhan, S.; Richey, B.; Anderson, C. F.; Record, M. T. Interaction of an N-methylated polyamine analogue, hexamethonium(2+), with sodium-DNA: quantitative nitrogen-14 and sodium-23 NMR relaxation rate studies of the cation-exchange process.

 Biochemistry 1988, 27, 4367–4376.
- (11) Burton, D. R.; Forsén, S.; Reimarsson, P. The interaction of polyamines with DNA: a 23 Na NMR study. *Nucleic Acids Res.* **1981**, *9*, 1219–1228.
- (12) Anderson, C. F.; Record, M. T. Polyelectrolyte Theories and their Applications to DNA. Annu. Rev. Phys. Chem. 1982, 33, 191–222.
- (13) Manning, G. S. Counterion binding in polyelectrolyte theory. Acc. Chem. Res. 1979, 12, 443–449.
- (14) Rouzina, I.; Bloomfield, V. A. Competitive Electrostatic Binding of Charged Ligands to Polyelectrolytes: Planar and Cylindrical Geometries. J. Phys. Chem. 1996, 100, 4292–4304.
- (15) Braunlin, W. H.; Anderson, C. F.; Record Jr., M. T. 23Na-nmr investigations of counterion exchange reactions of helical DNA. *Biopolymers* **1986**, *25*, 205–214.
- (16) Jain, S.; Zon, G.; Sundaralingam, M. Base only binding of spermine in the deep groove of the A-DNA octamer d(GTGTACAC). *Biochemistry* **1989**, *28*, 2360–2364.

- (17) Williams, L. D.; Frederick, C. A.; Ughetto, G.; Rich, A. Ternary interactions of spermine with DNA: 4'-epiadriamycin and other DNA: anthracycline complexes. *Nucleic Acids Res.* **1990**, *18*, 5533–5541.
- (18) Bancroft, D.; Williams, L. D.; Rich, A.; Egli, M. The low-temperature crystal structure of the pure-spermine form of Z-DNA reveals binding of a spermine molecule in the minor groove. *Biochemistry* **1994**, *33*, 1073–1086.
- (19) Deng, H.; Bloomfield, V. A.; Benevides, J. M.; Jr, G. J. T. Structural basis of polyamine–DNA recognition: spermidine and spermine interactions with genomic B-DNAs of different GC content probed by Raman spectroscopy. *Nucleic Acids Res.* 2000, 28, 3379–3385.
- (20) Ruiz-Chica, J.; Medina, M.; Sánchez-Jiménez, F.; Ramírez, F. Fourier Transform Raman Study of the Structural Specificities on the Interaction between DNA and Biogenic Polyamines. *Biophys. J.* 2001, 80, 443–454.
- (21) Bertoluzza, A.; Fagnano, C.; Finelli, P.; Morelli, M. A.; Simoni, R.; Tosi, R. Raman and infrared spectra of spermidine and spermine and their hydrochlorides and phosphates as a basis for the study of the interactions between polyamines and nucleic acids. J. Raman Spectrosc. 1983, 14, 386–394.
- (22) Dierksen, M.; Grimme, S. Density functional calculations of the vibronic structure of electronic absorption spectra. *J. Chem. Phys.* **2004**, *120*, 3544–3554.
- (23) Hart, S. M.; Silva, W. R.; Frontiera, R. R. Femtosecond stimulated Raman evidence for charge-transfer character in pentacene singlet fission. *Chem. Sci.* **2018**, *9*, 1242–1250.
- (24) Li, R.; Zheng, J.; Truhlar, D. G. Density functional approximations for charge transfer excitations with intermediate spatial overlap. *Phys. Chem. Chem. Phys.* **2010**, *12*, 12697–12701.

- (25) Silva, R.; Gichuhi, W. K.; Kislov, V. V.; Landera, A.; Mebel, A. M.; Suits, A. G. UV Photodissociation of Cyanoacetylene: A Combined Ion Imaging and Theoretical Investigation. J. Phys. Chem. A. 2009, 113, 11182–11186, PMID: 19827850.
- (26) 2022; https://cccbdb.nist.gov/vibscalejust.asp.
- (27) Jamróz, M. H. Vibrational Energy Distribution Analysis (VEDA): Scopes and limitations. Spectrochim. Acta A Mol. Biomol. Spectrosc. 2013, 114, 220–230.
- (28) Li, S.; Olson, W. K.; Lu, X.-J. Web 3DNA 2.0 for the analysis, visualization, and modeling of 3D nucleic acid structures. *Nucleic Acids Res.* **2019**, 47, W26–W34.
- (29) Suh, J.; Paik, H.; Hwang, B. Ionization of Poly(ethylenimine) and Poly(allylamine) at Various pH's. *Bioorg. Chem.* **1994**, *22*, 318–327.
- (30) Sun, C.; Tang, T.; Uludağ, H.; Cuervo, J. Molecular Dynamics Simulations of DNA/PEI Complexes: Effect of PEI Branching and Protonation State. *Biophys. J.* **2011**, *100*, 2754–2763.
- (31) Izadi, S.; Anandakrishnan, R.; Onufriev, A. V. Building Water Models: A Different Approach. J. Phys. Chem. Lett. **2014**, 5, 3863–3871.
- (32) Essmann, U.; Perera, L.; Berkowitz, M. L.; Darden, T.; Lee, H.; Pedersen, L. G. A smooth particle mesh Ewald method. J. Chem. Phys. 1995, 103, 8577–8593.
- (33) Ryckaert, J.-P.; Ciccotti, G.; Berendsen, H. J. Numerical integration of the Cartesian equations of motion of a system with constraints: molecular dynamics of n-alkanes. *J. Comput. Phys.* **1977**, *23*, 327–341.
- (34) Zgarbová, M.; Sponer, J.; Otyepka, M.; Cheatham, T. E.; Galindo-Murillo, R.; Jurečka, P. Refinement of the Sugar-Phosphate Backbone Torsion Beta for AMBER Force Fields Improves the Description of Z- and B-DNA. J. Chem. Theory Comput. 2015, 11, 5723-5736.

- (35) Case, D.; Belfon, K.; Ben-Shalom, I.; Brozell, S.; Cerutti, D.; Cheatham, T.; Cruzeiro, V.; Darden, T.; Duke, R.; Giambasu, G. et al. *Amber 2020*; WorkingPaper, 2020.
- (36) Michaud-Agrawal, N.; Denning, E. J.; Woolf, T. B.; Beckstein, O. MDAnalysis: A toolkit for the analysis of molecular dynamics simulations. *J. Comput. Chem.* **2011**, 32, 2319–2327.
- (37) Gowers, R. J.; Linke, M.; Barnoud, J.; Reddy, T. J. E.; Melo, M. N.; Seyler, S. L.; Domanski, J.; Dotson, D. L.; Buchoux, S.; Kenney, I. M. et al. MDAnalysis: A Python Package for the Rapid Analysis of Molecular Dynamics Simulations. **2016**,
- (38) Humphrey, W.; Dalke, A.; Schulten, K. VMD: Visual molecular dynamics. J. Mol. Graph. 1996, 14, 33–38.
- (39) Berendsen, H.; van der Spoel, D.; van Drunen, R. GROMACS: A message-passing parallel molecular dynamics implementation. *Comput. Phys. Commun.* **1995**, *91*, 43–56.
- (40) Mintzer, M. A.; Simanek, E. E. Nonviral Vectors for Gene Delivery. *Chem. Rev.* **2009**, 109, 259–302.
- (41) 2014; https://www.polysciences.com/default/polyethylenimine-linear-mw-2500.
- (42) York, S. S.; Boesch, S. E.; Wheeler, R. A.; Frech, R. Vibrational Assignments for High Molecular Weight Linear Polyethylenimine (LPEI) Based on Monomeric and Tetrameric Model Compounds. *Macromolecules* 2003, 36, 7348–7351.
- (43) Sanchez-Cortes, S.; Berenguel, R. M.; Madejón, A.; Pérez-Méndez, M. Adsorption of Polyethyleneimine on Silver Nanoparticles and Its Interaction with a Plasmid DNA: A Surface-Enhanced Raman Scattering Study. *Biomacromolecules* **2002**, *3*, 655–660.

- (44) Emin, A.; Hushur, A.; Mamtimin, T. Raman study of mixed solutions of methanol and ethanol. *AIP Adv.* **2020**, *10*, 065330.
- (45) Bykov, S.; Asher, S. Raman Studies of Solution Polyglycine Conformations. *J. Phys. Chem. B* **2010**, *114*, 6636–6641.
- (46) Bykov, S. V.; Asher, S. A. UV Resonance Raman Elucidation of the Terminal and Internal Peptide Bond Conformations of Crystalline and Solution Oligoglycines. J. Phys. Chem. Lett. 2010, 1, 269–271.
- (47) Hashida, T.; Tashiro, K.; Aoshima, S.; Inaki, Y. Structural Investigation on Water-Induced Phase Transitions of Poly(ethylene imine). 1. Time-Resolved Infrared Spectral Measurements in the Hydration Process. *Macromolecules* **2002**, *35*, 4330–4336.
- (48) Gaber, B. P.; Peticolas, W. L. On the quantitative interpretation of biomembrane structure by Raman spectroscopy. *Biochimica et Biophysica Acta (BBA) Biomembranes* 1977, 465, 260–274.
- (49) Strobl, G.; Hagedorn, W. Raman Spectroscopic Method for Determining the Crystallinity of Polyethylene. J. Polym. Sci. B Polym. Phys. 1978, 16, 1181–1193.
- (50) Wool, R.; Bretzlaff, R.; Li, B.; Wang, C.; Boyd, R. Infrared and Raman Spectroscopy of Stressed Polyethylene. *J Polym. Sci. B Polym. Phys.* **1986**, *24*, 1039–1066.
- (51) Farber, C.; Li, J.; Hager, E.; Chemelewski, R.; Mullet, J.; Rogachev, A. Y.; Kurouski, D. Complementarity of Raman and Infrared Spectroscopy for Structural Characterization of Plant Epicuticular Waxes. ACS Omega 2019, 4, 3700–3707.
- (52) Schneider, S. H.; Boxer, S. G. Vibrational Stark Effects of Carbonyl Probes Applied to Reinterpret IR and Raman Data for Enzyme Inhibitors in Terms of Electric Fields at the Active Site. J. Phys. Chem. B 2016, 120, 9672–9684.

- (53) Jones, R. N.; Angell, C. L.; Ito, T.; Smith, R. J. D. The carbonyl stretching bands in the infrared spectra of unsaturated lactones. *Can. J. Chem.* **1959**, *37*, 2007–2022.
- (54) Inuzuka, K.; Ito, M.; Imanishi, S. Effect of Solvent on Carbonyl Stretching Frequency of Ketones. *Bull. Chem. Soc. Jpn.* **1961**, *34*, 467–471.
- (55) Wang, Y.; Purrello, R.; Georgiou, S.; Spiro, T. G. UVRR Spectroscopy of the Peptide Bond. 2. Carbonyl H-Bond Effects on the Ground- and Excited-State Structures of N-methylacetamide. J. Am. Chem. Soc. 1991, 113, 6368–6377.
- (56) Punihaole, D.; Jakubek, R. S.; Workman, R. J.; Asher, S. A. Interaction Enthalpy of Side Chain and Backbone Amides in Polyglutamine Solution Monomers and Fibrils. J. Phys. Chem. Lett. 2018, 9, 1944–1950.
- (57) Hong, Z.; Wert, J.; Asher, S. A. UV Resonance Raman and DFT Studies of Arginine Side Chains in Peptides: Insights into Arginine Hydration. J. Phys. Chem. B 2013, 117, 7145–7156.
- (58) Punihaole, D.; Jakubek, R. S.; Dahlburg, E. M.; Hong, Z.; Myshakina, N. S.; Geib, S.; Asher, S. A. UV Resonance Raman Investigation of the Aqueous Solvation Dependence of Primary Amide Vibrations. J. Phys. Chem. B 2015, 119, 3931–3939.
- (59) Eckhardt, G.; Wagner, W. G. On the calculation of absolute Raman scattering cross sections from Raman scattering coefficients. *J. Mol. Spectrosc.* **1966**, *19*, 407–411.
- (60) Nestor, J. R.; Lippincott, E. R. The effect of the internal field on Raman scattering cross sections. *J. Raman Spectrosc.* **1973**, *1*, 305–318.
- (61) Placzek, G. Rayleigh-Streuung und Raman-Effekt; 1934.
- (62) Schrötter, H.; Bernstein, H. Absolute Raman intensities. J. Mol. Spectrosc. 1961, 7, 464–465.

- (63) Schrötter, H.; Bernstein, H. Intensity in the Raman effect. IX. Absolute intensities for some gases and vapors. J. Mol. Spectrosc. 1964, 12, 1–17.
- (64) Owen, B. B.; Miller, R. C.; Milner, C. E.; Cogan, H. L. The Dielectric Constant of Water as a Function of Temperature and Pressure. *J. Phys. Chem.* **1961**, *65*, 2065–2070.
- (65) https://depts.washington.edu/eooptic/linkfiles.
- (66) Dudik, J. M.; Johnson, C. R.; Asher, S. A. Wavelength dependence of the preresonance Raman cross sections of CH₃CN, SO₄²⁻ClO₄⁻and NO₃⁻. *J. Phys. Chem. B* **1985**, *82*, 1732–1740.
- (67) Ruiz-Chica, J.; Medina, M.; Sánchez-Jiménez, F.; Ramírez, F. Raman Study of the Interaction between Polyamines and a GC Oligonucleotide. *Biochem. Biophys. Res. Commun.* **2001**, *285*, 437–46.
- (68) Peticolas, W. L. Raman spectroscopy of DNA and proteins. 1995, 246, 389–416.
- (69) Benevides, J. M.; Stow, P. L.; Ilag, L. L.; Incardona, N. L.; Thomas, G. J. Differences in secondary structure between packaged and unpackaged single-stranded DNA of bacteriophage .vphi.X174 determined by Raman spectroscopy: a model for .vphi.X174 DNA packaging. *Biochemistry* **1991**, *30*, 4855–4863.
- (70) Thomas, G. J.; Wang, A. H.-J. In *Nucleic Acids and Molecular Biology*; Eckstein, F., Lilley, D. M. J., Eds.; Springer Berlin Heidelberg: Berlin, Heidelberg, 1988; pp 1–30.
- (71) Thomas, G. J.; Hartman, K. A. Raman studies of nucleic acids VIII estimation of RNA secondary structure from raman scattering by phosphate-group vibrations. *Biochim. Biophys. Acta., Proteins Proteomics* **1973**, *312*, 311–322.
- (72) Duguid, J.; Bloomfield, V.; Benevides, J.; Thomas, G. DNA melting investigated by differential scanning calorimetry and Raman spectroscopy. *Biophys. J.* **1996**, *71*, 3350–3360.

(73) Cuervo, A.; Dans, P. D.; Carrascosa, J. L.; Orozco, M.; Gomila, G.; Fumagalli, L. Direct measurement of the dielectric polarization properties of DNA. *Proc. Natl. Acad. Sci. U.S.A.* **2014**, *111*, E3624–E3630.

Pentaethylenehexamine (PEHA)
$$H_{2}N \xrightarrow{N} N \xrightarrow{N} N \xrightarrow{N} NH_{2}$$

$$Tetraethylenepentamine (TEPA)$$

$$H_{2}N \xrightarrow{N} N \xrightarrow{N} NH_{2}$$

$$Diethylenetriamine (DETA)$$

$$H_{2}N \xrightarrow{N} NH_{2}$$

N-Ethylpropylamine (NEPA)
$$H_3C \overset{\textstyle \wedge}{\underset{\displaystyle H}{\wedge}} \overset{\textstyle CH_3}{\underset{\displaystyle H}{\wedge}}$$

Figure 1: Schematic of model compounds used in this study.

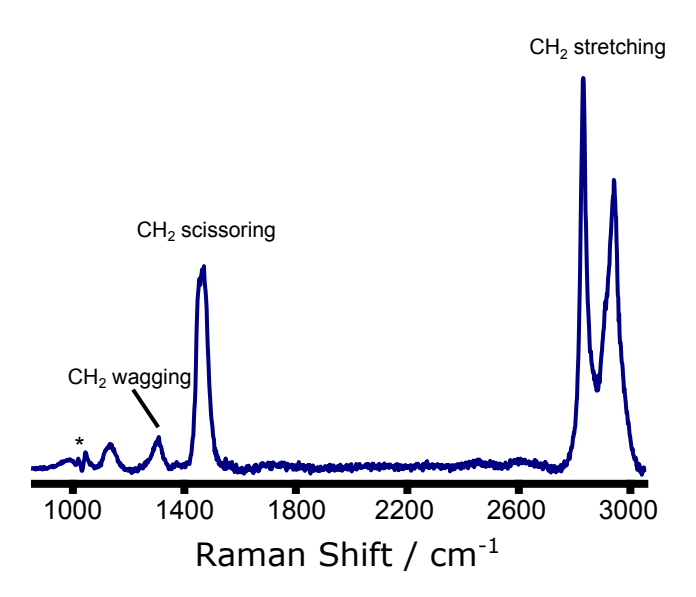


Figure 2: Raman spectrum of high molecular weight PEI (2500 Da) prepared at 30 mM in methanol. The spectroscopic contribution of methanol has been subtracted out. The asterisk (*) symbol shows an artifact of subtracting out the spectral contribution of methanol.

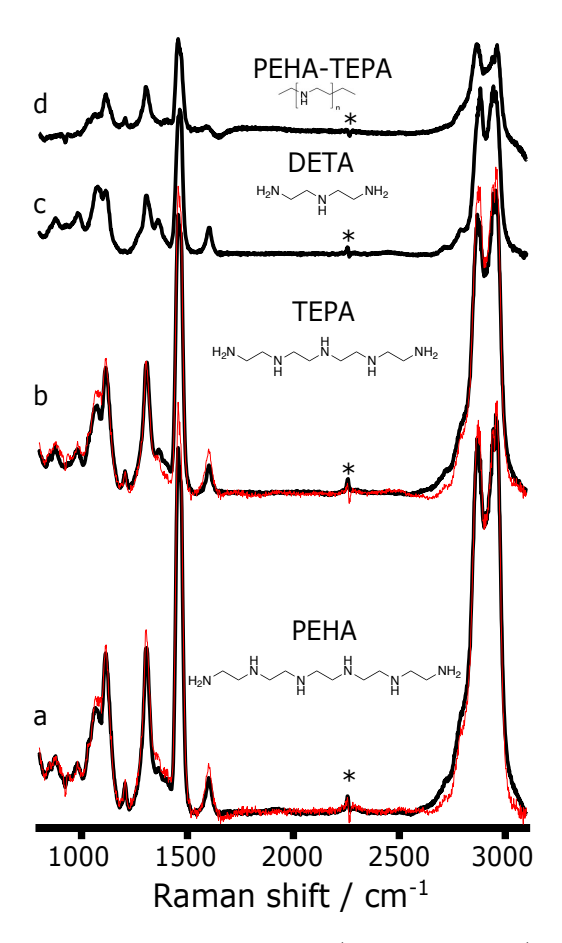


Figure 3: Raman spectra of low molecular weight (103-232 Da) PEIs prepared at equimolar (200 mM) concentrations in water. (a) PEHA (black trace); (b) TEPA (black trace); (c) DETA; (d) PEHA - TEPA difference spectrum. The difference spectrum closely approximates the spectrum of internal monomers in PEIs, while the DETA spectrum approximates the spectrum of terminal monomers. This is demonstrated by the fact that the PEHA and TEPA spectra can be modeled as a linear combination of the spectra shown in (c) and (d). PEHA can satisfactorily modeled as $3\times(\text{PEHA} - \text{TEPA}) + \text{DETA}$ (red trace in panel a), while TEPA can be modeled as $2\times(\text{PEHA} - \text{TEPA}) + \text{DETA}$ (red trace in panel b). All spectra were normalized to the $2250 \, \text{cm}^{-1}$ nitrile stretching band of acetonitrile, which was used as an internal intensity standard. The spectral contribution of solvent was subtracted out. The asterisk (*) symbol shows an artifact of subtracting out the spectral contribution of the nitrile stretching band of acetonitrile.

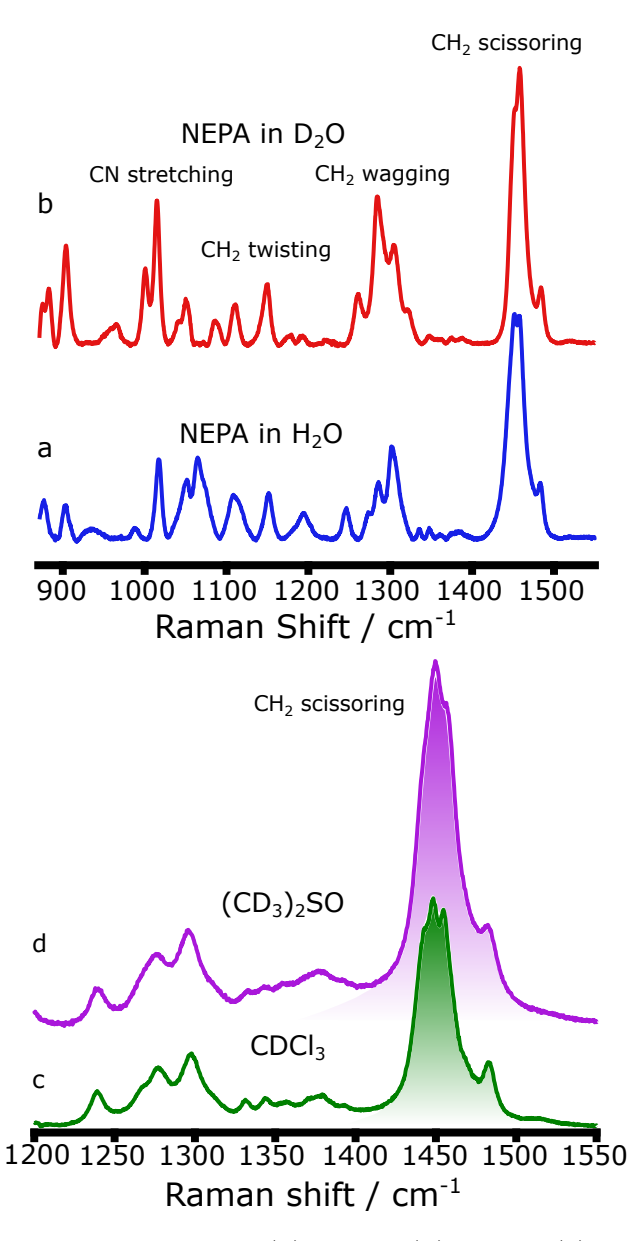


Figure 4: Raman spectra of NEPA in: (a) H_2O ; (b) D_2O ; (c) $CDCl_3$; and $(CD_3)_2SO$. All spectra were measured using a high-resolution (2400 gr/mm) grating. The spectral contributions of solvents were subtracted from all spectra. For (c) and (d), the Raman bands that derive from CH_2 scissoring modes are highlighted to show the intensity changes that occur between low and high dielectric environments.

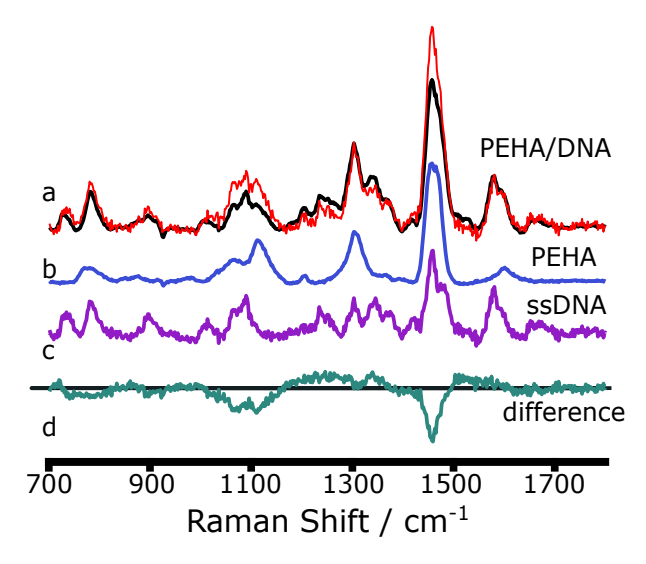


Figure 5: Raman spectra of: (a) PEHA (100 mM)-ssDNA (3 mM) in solution (black trace); (b) PEHA (100 mM); and (c) ssDNA (3 mM). The red trace in (a) is the sum of the spectra shown in (c) and (d). The difference spectrum shown in (d) was calculated by subtracting the red trace from the black trace in (a). The fact that the experimentally measured spectrum in (a) shown in the black trace cannot be modeled as a linear combination of the ssDNA (c) and PEHA (b) spectra indicates binding is occurring between the two species. All spectra were normalized to the 2250 cm⁻¹ nitrile stretching band of acetonitrile, which was used as an internal intensity standard. The asterisk (*) symbol shows an artifact of subtracting out the spectral contribution of this nitrile stretching band.

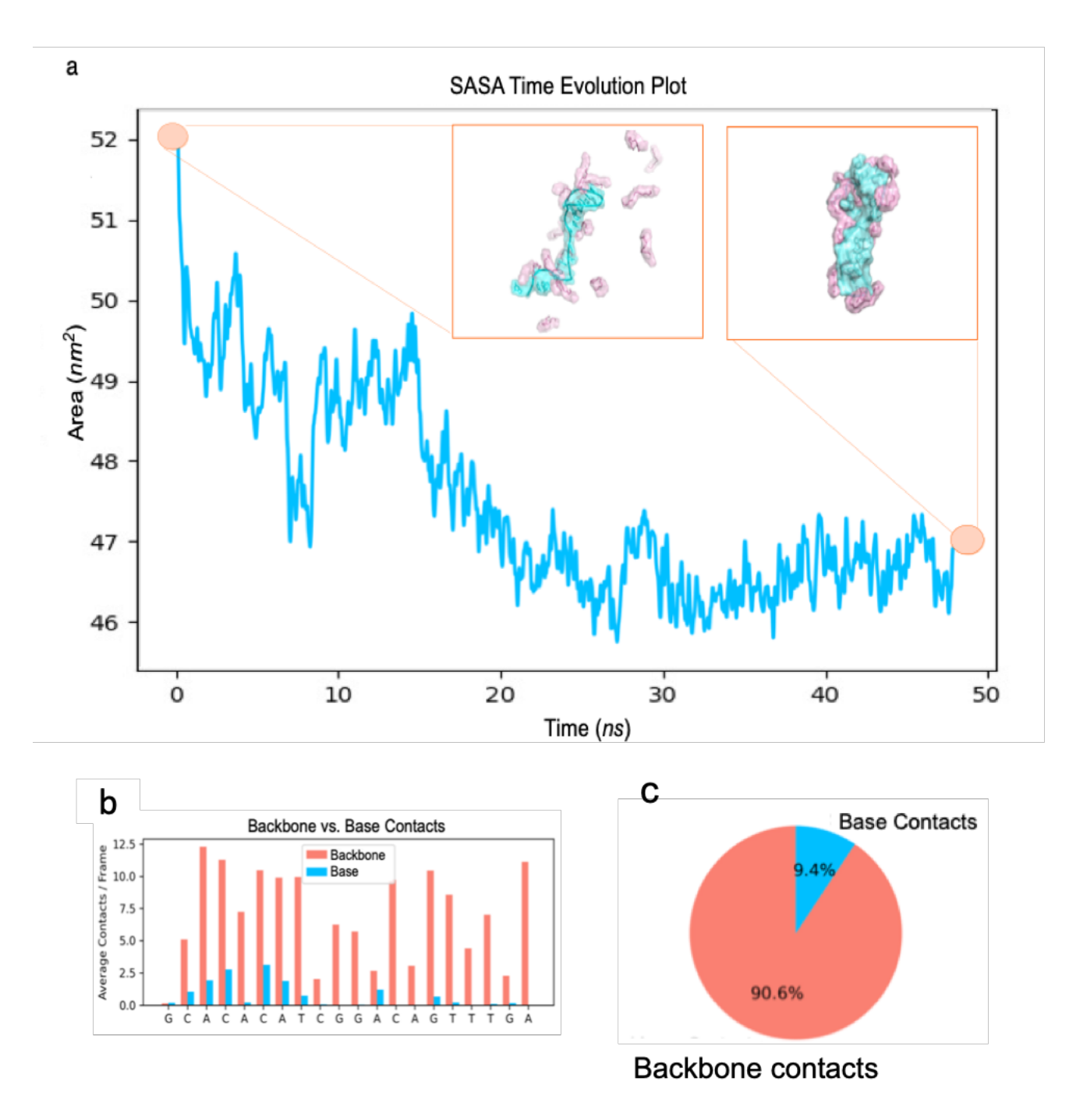


Figure 6: MD simulation results of PEHA binding ssDNA in water. (a) Solvent accessible surface area (SASA) time evolution plot. Structures are inlayed corresponding to before and after the confirmational change. Disordered secondary structure is established with polymer bound to the DNA surface. (b) Ratio per residue of backbone contacts vs. base contacts (4 Å cutoff, averaged over total frames). (c) Pie chart of overall backbone/base interactions. The chart shows PEHA exhibits a higher affinity for the DNA backbone (electrostatics) than for the DNA bases (hydrogen bonding). Polymer binding sites correspond to areas of high electrostatic potential shown in Figure S8a.

Table 1: Frequencies (cm $^{-1}$) and Assignments of Raman Bands for NEPA, DETA, TEPA, and PEHA

NEPA	DETA	TEPA.	РЕНА	Assignment	
-	1601	1601	1601	NH_2 bend	
1484	-	-	-	CH_3 def + CH_2 scissors	
1467	1466	1467	1467	CH_2 scissors + NH bend	
1459	1457	1457	1457	CH_2 scissors + NH bend	
1452	-	-	-	CH_2 scissors	
1443		-	-	CH_3 def + CH_2 scissors	
-	-	1388	1388	CH_2 wag	
-	1361	1363	1363	CH_2 wag	
1303	1304	1304	1304	CH_2 wag	
1286	-	-	-	CH_3 wag	
1274	-	-	-	CH ₂ twist	
1247	-	-	-	CH_2 twist	
-		1204	1204	CH ₂ twist	

36

Table 2: Comparison of Differential Raman Cross Sections $(d\sigma_i/d\Omega)$ of NEPA in Different Solvents

	$d\sigma_i/d\Omega \ (\times 10^{-4})^a$			Cross section ratio^b		
Raman shift (cm^{-1})	$\mathrm{H_{2}O}$	CDCl_3	$(CD_3)_2SO$	$\overline{\mathrm{CDCl_3/(CD_3)_2SO}}$	$(\mathrm{CD_3})_2\mathrm{SO/H_2O}$	
1443	4.241 ± 0.066	4.908 ± 0.004	7.480 ± 0.010	0.722 ± 0.002	1.164 ± 0.016	
1448	9.866 ± 0.274	4.910 ± 0.006	7.686 ± 0.015	0.703 ± 0.002	0.514 ± 0.028	
1455	7.967 ± 0.414	5.670 ± 0.005	8.338 ± 0.010	0.749 ± 0.001	0.691 ± 0.052	
1467	3.422 ± 0.109	1.278 ± 0.002	1.772 ± 0.005	0.794 ± 0.003	0.342 ± 0.032	
1483	1.785 ± 0.070	1.868 ± 0.001	2.588 ± 0.003	0.794 ± 0.001	0.957 ± 0.039	

 $[^]a$ units are mb sr $^{-1}$ molec. $^{-1}$; b ratio = $\frac{L_j(d\sigma/d\Omega)_k}{L_k(d\sigma/d\Omega)_j}$, where j and k are solvents. $L_{H_2O} = 2.52$, $L_{(CD_3)_2SO} = 3.82$, $L_{CDCl_3} = 3.47$